Selective inhibitory activity of multidrug-resistant bacteria by zinc oxide nanoparticles

Gleison N. Marques [a], Ailton José Moreira [b], Eryka Thamyris D. Nóbrega [a], Sandalene Braga [c], Marcela N. Argentin [d], Ilana L.B. da Cunha Camargo [d], Emilio Azevedo [c], Ernesto C. Pereira [a], Maria Inês B. Bernardi [e],[*], Lucia H. Mascaro [a]

[a] *CDMF, LIEC, Universidade Federal de São Carlos (UFSCar), 13565-905 São Carlos, SP, Brazil*
[b] *Instituto de Química (IQ), Universidade Estadual Paulista (UNESP), 14800-900 Araraquara, SP, Brazil*
[c] *Instituto Federal de Educação, Ciência e Tecnologia do Maranhão (IFMA), Monte Castelo, 65030-005 São Luís, MA, Brazil*
[d] *Laboratório de Epidemiologia e Microbiologia Moleculares, Departamento de Física e Ciências Interdisciplinares, Instituto de Física de São Carlos, Universidade de São Paulo, São Paulo, SP, Brazil*
[e] *Instituto de Física de São Carlos, Universidade de São Paulo (IFSC-USP), 13560-970 São Carlos, SP, Brazil*

ARTICLE INFO

ABSTRACT

The emergence of multidrug-resistant bacteria has attracted much attention from the global community due to their potential to cause harm to health. In this context, ZnO nanoparticles (NPs) produced under different synthesis conditions were successfully applied to inhibit several species of multiresistant bacteria from clinical isolates. Five gram-positive (*Staphylococcus epidermidis* ATCC 35984, *Staphylococcus aureus* ATCC 25923, *S. aureus* ATCC 8095, *Enterococcus faecalis* ATCC 29212, and *Enterococcus faecium* ATCC 700221) and four gram-negative bacterial isolates (*Klebsiella pneumoniae* ATCC 700603, *Escherichia coli* ATCC 25922, *Acinetobacter baumannii* ATCC 19606, and *Pseudomonas aeruginosa* ATCC 27853), known to be involved in healthcare-associated infections and multidrug resistance, were selected for this study. Due to their physicochemical properties, we found that ZnO NPs can exhibit selective inhibition. The minimum inhibitory concentration (MIC) for multidrug-resistant bacteria sensitive to ZnO NPS was determined from varying contact time and catalyst concentration from exhaustive tests. Different characterization techniques were studied to determine the crystalline, optical, morphological, and photocatalytic characteristics of ZnO NPs. The bacterial inhibition mechanisms were discussed in detail with support of photocatalytic assays and cytotoxicity of plant species. In addition, ZnO NPs have also shown great potential for application in the environmental remediation of ecosystems contaminated by organic pollutants due to their efficiency in degrading the dye methylene blue (MB) under UV light with a photocatalytic efficiency of 75% in 60 min. The ZnO NPs showed great potential for multidrug-resistant bacteria, with MICs ranging from 256 to 512 mg/L. This demonstrates that the ZnO NPs produced here have the potential to be used as a technology with great application potential in materials used in hospital environments to mitigate the growth and development of these classes of multi-resistant bacteria.

1. Introduction

In recent years, the number of multidrug-resistant bacteria has been increasing, partly due to the widespread use of antimicrobials and improper disposal of these drugs [1]. The ESKAPE (*Enterococcus faecium, Staphylococcus aureus, Klebsiella pneumoniae, Acinetobacter baumannii, Pseudomonas aeruginosa,* and *Enterobacter* spp.) group, for example, generates great concern due to the variety of strains capable of causing damage to health and acquiring drug resistance genes [2,3]. The search for strategies capable of mitigating and controlling the growth of diseases caused by these microorganisms has gained much attention due to the decreased available therapeutic options [4–6].

Recent advances in nanotechnology have proven the efficiency of using metallic nanoparticles (NPs) or their oxides in controlling the risks of contamination by pathogenic microorganisms [7–10]. Because they have distinct cell structures, the antibacterial effect of NPs often depends

on specific characteristics of the material, which act selectively [11,12]. The main mechanisms involved in the antimicrobial action of NPs are the release of ions, direct contact with the NPs by electrostatic interaction, and the indirect mechanism by reactive oxygen species (ROS) formation. All these mechanisms can damage the cell membrane and inactivate the bacteria [13,14].

Despite the excellent results presented mainly by NPs of Au and Ag, using these noble metals can make the production of functionalized materials from them more expensive and bump into environmental, health, and safety aspects related to their bioaccumulation and toxicity [15]. On the other hand, zinc oxide nanoparticles (ZnO-NPs) have excellent antibacterial, antifungal, and anti-inflammatory properties and a low cytotoxic effect [16–20]. In addition to antimicrobial activity, ZnO NPs have also been explored in other areas, such as photocatalysis in tests involving the degradation of organic compounds in aquatic environments and analytical methodologies for environmental monitoring [21].

To improve the properties of ZnO-NPs, some studies have observed that the control of morphology, lattice parameters, and the formation of defects can be achieved by changing the synthesis method, metallic precursors, or pH of the medium [22–27]. Gonzalez et al. [28] observed that changing the morphology of ZnO NPs (spherical, hexagonal, and rod shapes) significantly affected antibacterial and anticancer activity. Mainly, NPs with spherical shapes showed more excellent biocide effects than hexagonal particles, increasing oxidative stress and apoptosis in cancer cells. Literature data show that particles with larger crystallite sizes can exhibit better photocatalytic activity [29], and ZnO nanoparticles can produce ROS even in the dark [30]. However, in the presence of light, this production is optimized by the photocatalytic process [31]. Besides being widely applied in the degradation of organic pollutants, this photocatalytic property also improves the bactericidal efficiency of the material through the ROS inactivation mechanism[32].

The microwave-assisted hydrothermal method (HaM) has proven effective in producing various NPs[33]. The HaM promotes uniform, fast, and easy-to-control heating in which variables such as temperature, irradiation time, and pressure can be easily changed and investigated through experimental design approaches [23]. Gusmão et al. [27] observed that the change in the morphology of pure and Ag-doped ZnO using the HaM method depends on the alkaline medium in which the nucleation process occurs. When comparing the biocidal effect of ZnO obtained with NaOH and the material produced using NH$_4$OH, pure samples show more significant antimicrobial activity against *Saccharomyces cerevisiae* observed by the medium containing ammonium hydroxide at pH 12. In addition, using different Zn^{2+} salt precursors can guide preferential growth along axial or radial directions due to the different ZnO facets' interaction with the metal precursors' anions [34].

In this work, ZnO-NPs were produced using the HaM. A factorial planning study was conducted to investigate the influence of experimental parameters, such as the type of metal precursor, the alkaline medium using different bases, and the microwave irradiation time. These parameters can play a significant role in modifying the properties of ZnO NPs, including their antibacterial, photocatalytic, and phytotoxic properties. By varying these parameters, it is possible to obtain ZnO NPs with specific characteristics that can improve their antibacterial efficacy, enhance their photocatalytic activity, or influence their toxicity to living organisms. Therefore, understanding the influence of these parameters is crucial to optimizing the desired properties of ZnO NPs for relevant applications.

2. Experimental section

2.1. Synthesis and characterization of ZnO NPs

In the preparation of the ZnO NPs, 50 mL of the (Zn(NO$_3$)$_2$·6 H$_2$O or Zn(CH$_3$COO)$_2$·2 H$_2$O) solution, at a concentration of 0.06 M prepared with deionized water, was added in a beaker and kept under stirring at

60 °C for 20 min. Subsequently, 50 mL of a 1.2 M alkaline solution (NaOH or NH$_4$OH) was continuously dropped into the salt solution. During this process, the color change of the solution was observed as the ZnO precipitates were being formed. Then, the resulting solution was transferred to a Teflon-lined stainless-steel autoclave (100 mL) and heat treated in a microwave at 120 °C for different times (15 or 30 min). The white precipitate from this process was washed successively with distilled water and ethanol to remove impurities and then dried in an oven at 60 °C for 24 h. All reagents used in the synthesis of ZnO were of analytical grade. The samples produced were identified as shown in Table 1.

The analysis of the crystalline structure of the powders was performed from X-ray diffraction (XRD) using a Shimadzu diffractometer model XRD-6100 with a range of 10–110º (2θ) voltage of 40 kV and a rate of 0.05 °/s. An additional study of the ZnO phase to investigate possible changes in the network parameters of the materials was carried out from the Rietveld refinement using the General Structure Analysis System II (GSAS II) software [35]. The values determined for the crystallite sizes of each sample were calculated using the Scherrer Equation [36]. The NPs' morphology was observed using scanning electron microscopy by field emission (FE-SEM) using a ZEISS model SIGMA microscope. Compositional analysis of the chemical elements in the samples was performed by dispersive X-ray spectroscopy (EDS) using an accelerating voltage of 10 and 20 kV on a Hitachi microscope, TM4000 Plus, with an integrated backscattered electron detector (BSE). The band gap values of the materials were calculated from the Kubelka-Munk method using the UV–vis spectra obtained using a Cary 7000 spectrophotometer coupled with an integrating sphere in the diffuse reflectance (DRS) mode in the region between 200 - 800 nm [37]. Zeta potential was respectively measured on a Malvern Zetasizer® nanoZS-equipment in pH = 6.5 (no adjustment).

2.2. Screening of antibacterial activity

The antimicrobial activity of ZnO NPs was evaluated against Gram-positive *S. epidermidis*, *S. aureus* ATCC 25923, *S. aureus* ATCC 8095, *E. faecalis* ATCC 29212, *E. faecium* ATCC 700221 and Gram-negative, *K. pneumoniae* ATCC 700603, *E. coli* 25922, *A. baumannii* ATCC 19606, and *P. aeruginosa* ATCC 27853 bacteria. Some of these bacteria are representative of the ESKAPE group, responsible for severe infections, and have become resistant to many antibiotics. Because of this, the WHO lists most as critical and priority pathogens [38]. To study the antibacterial activity of different ZnO NPs, 5120 mg/L of the powders were prepared by dispersion in water and autoclaved to avoid contamination. Subsequently, the stock suspension was diluted at a ratio of 1:10 in Mueller Hinton Cation Adjusted Broth (MHCA) (BD, East Rutherford, NJ, USA) containing Biolog Redox Dye Mix H (100x) (Biolog, Hayward, CA, USA) at a ratio of 1.05%. After that, bacterial inoculum at the final concentration of 10^5 CFU/mL was added to each 512 mg/L ZnO NPs in a final volume of 100 μL in a 96-well microdilution plate. The bacteria were grown in MHCA broth without ZnO NPs for positive control. The MHCA broth without the bacteria and ZnO NPs were incubated to show no contamination as a negative control. The incubation was performed

Table 1
Identification of the samples and characteristics related to each synthesis.

Identification samples	Characteristic		
	Metallic precursor	Base	Irradiation time (min)
ZnO – 1	Zn(NO$_3$)$_3$	NaOH	15
ZnO – 2	Zn(NO$_3$)$_3$	NaOH	30
ZnO – 3	Zn(CH$_3$COO)$_2$	NaOH	15
ZnO – 4	Zn(CH$_3$COO)$_2$	NaOH	30
ZnO – 5	Zn(NO$_3$)$_3$	NH$_4$OH	15
ZnO – 6	Zn(NO$_3$)$_3$	NH$_4$OH	30
ZnO – 7	Zn(CH$_3$COO)$_2$	NH$_4$OH	15
ZnO – 8	Zn(CH$_3$COO)$_2$	NH$_4$OH	30

at 36 °C ± 1 °C, and the reading of the results was done using the OmniLog® (Biolog, Hayward, CA) equipment every 15 min in the period of 24 h using Biolog's OmniLog Data Collection v. 3.0 software [39]. From the colorimetric signal captured by the OmniLog device (OmniLog units, OU) at various time intervals during the screening test, kinetic metabolism curves (OU x time) were plotted for each bacterium analyzed. The screening was considered positive in the absence of bacterial metabolism, indicating the antibacterial activity at the concentration tested. The positive screening result in this case was ≤ 512 mg/L. In the presence of bacterial metabolism, the screening was considered negative, indicating the absence of antibacterial activity at the concentration tested. The negative screening does not exclude the possibility that this compound exhibits antibacterial activity at higher concentrations, so the result is expressed as "> 512 mg/L". All assays were performed in triplicate, and both controls received Biolog Redox Dye Mix H (100 ×) in the same proportion.

2.3. Determination of the minimum inhibitory concentration (MIC)

After a screening step, the ZnO NPs that inhibited the bacterial metabolism at 512 mg/L were tested against these bacterial isolates to determine the MIC. Daptomycin and imipenem (Gold Biotechnology, St. Louis, MO, USA) were antibiotics used as controls against the gram-positive and gram-negative bacterial isolates, respectively. Daptomycin stock solution and broth were prepared as CLSI (2013) recommended. Serial dilutions (1:2) from the ZnO NPs, daptomycin and imipenem at 512 mg/L were prepared up to 0.06 mg/L in MHCA broth plus 1 × Biolog Redox Dye Mix H. Each dilution was tested against 10^5 CFU/mL of each bacteria in a final volume of 100 μL in a 96-well microplate to determine the ZnO NPs MIC. The microplates were incubated in the OmniLog® (Biolog, Hayward, CA, USA) apparatus at 36 °C ± 1 °C for 24 h, with readings registered every 15 min, followed by a final visual observation of the plates to follow the metabolism kinetics of the bacteria. MIC was considered the lowest compound concentration able to inhibit the bacterium metabolism. In the positive control, bacteria were added to the broth without ZnO-NPs to show they could grow in MHCA broth. In the negative control, there was only MHCA broth, without bacteria, to prove no broth contamination occurred; both controls also received 1 × Biolog Redox Dye Mix H. All assays were performed in triplicate.

2.4. Photocatalytic activity

In a 100 mL glass beaker, 50 mg of photocatalyst and 50 mL of MB 20 mg/L solution were added. The mixture was kept under stirring in the dark for 30 min to reach adsorption-desorption equilibrium and then irradiated for up to 60 min in a reactor containing 6 lamps UV-C lamps (254 nm). Details of the reactor used in this study can be found in [40]. At each 10 min interval, an aliquot of the sample (1 mL) was taken and subjected to centrifugation to separate the catalyst and the supernatant analyzed by UV-Vis spectrophotometry in scanning mode applying a wavelength range of 500 to 700 nm. To investigate degradation mechanisms, studies using 2 mmol silver nitrate (AgNO₃ - Sigma-Aldrich ≥ 99.0%), *tert*-butanol [(CH₃)₃COH - Sigma-Aldrich ≥ 99.5%], methanol (CH₃OH, Sigma-Aldrich ≥ 99.8%), and 0.002 mol de p-benzoquinone (C₆H₄O₂ - Sigma-Aldrich ≥ 98.0%) as interfering/scavenger of reactive species of the electron, hydroxyl, hole, and superoxide types, respectively (e^-, OH⁻, h^+ and O₂⁻) [41]. In addition, the specific probe assay for hydroxyl radicals using coumarin was performed as described in the literature [42]. To follow Zn^{2+} leaching after 60 min of irradiation using the photocatalytic conditions described above, the samples were filtered through a 0.22 μm membrane, the filtrate transferred to a polypropylene tube, acidified to 1% (v v⁻¹) with nitric acid (Sigma Aldrich, 65%) and analyzed by flame atomic absorption spectroscopy (FAAS) using the same methodology described in Paris et al. [42].

2.5. Phytotoxicity

The effect of ZnO-NPs toxicity on the germination rate of *Cucumis sativus* (*C. sativus*) seeds and their root growth was investigated using a methodology adapted from Wang et al. [43]. Briefly, the seeds of *C. sativus* were previously disinfected with 4% sodium hypochlorite and then moistened with distilled water. Then, 10 seeds were placed on filter paper (90 mm – 80 g/m²) in sterile disposable Petri dishes (90 ×15 mm) and exposed to a solution of ZnO-NPs at a suspension of 512 μg/mL (the same maximum concentration used in the tests bactericidal). Petri dishes were wrapped with PVC plastic film and kept in a dark environment at a controlled temperature (25 ± 2 °C) for 5 days. The tests were performed in triplicate, and the same procedure was adopted in the case of the negative control tests, in this case, using distilled water.

2.6. Statistical treatment

Principal Component Analysis (PCA) is a widely employed statistical technique to uncover meaningful patterns and reduce the dimensionality of complex datasets [44]. In this study, particularly the analysis of MIC bacterial data, PCA offers a valuable approach to gaining insights from multidimensional information. The experimental procedure involved first collecting MIC values, which were organized into a matrix with antimicrobial agents as rows. PCA, using auto-scaling as a pre-processing, was the default method of data analysis. By performing PCA on this matrix, the variability in MIC values was transformed into a set of orthogonal components called principal components. Data import, pre-processing, and constructing multivariate models were performed within the R statistics platform (R Foundation for Statistical Computing) version 4.3.1 environment [45]. These components are ordered by the amount of variance they explain in the original data. This transformation highlights the most significant patterns and relationships between bacterial strains, antimicrobial agents, and MIC values.

3. Results and discussion

3.1. Antibacterial activity of the ZnO structures

To comprehend the antibacterial activity of ZnO nanostructures, it is imperative to initiate the analysis with a comprehensive characterization of these structures. To confirm the ZnO structure, Fig. 1 shows the XRD patterns of the samples produced using NaOH (Fig. 1a) or NH₄OH (Fig. 1b) in synthesis times of 15 and 30 min, applying nitrate or zinc acetate as a metallic precursor. Only peaks related to the wurtzite ZnO structure are observed (ICDD crystal chart no. 36–1451, space group P63mc), indicating, within the limit of detection of the technique, the absence of secondary phases [46].

From the kinetic metabolism curves of each bacterium analyzed at 512 mg/mL ZnO-NPs, presented in the Supplementary Material (Figs. S1 - S8), it was possible to determine whether there was antibacterial activity. The screening results demonstrated that the ZnO NPs showed only antibacterial activity against gram-positive bacteria, mostly against *S. epidermidis, S. aureus* (ATCC 25923), and *E. faecium*. Imipenem MICs for the gram-negative bacteria *K. pneumoniae, E. coli, A. baumannii,* and *P. aeruginosa* were 0.25, 0.25, 8, and 4 mg/L, respectively. The metabolism kinetics curves of the bacterial strains tested against several ZnO NPs concentrations were obtained from the OmniLog over 24 h and used to determine the MIC (Table 2).

To ensure that the ZnO NPS synthesized in this study are composed of the pure wurtzite phase, the Rietveld refinement was applied the fits obtained were satisfactory (Fig. S9). Through refinement, it was also possible to extract data on the structural parameters (*a,b,* and *c*) density and cell volume of the ZnO phases (Table 3) based on a CIF file obtained from the Inorganic Crystal Structure Database. (ICSD) nº 26170.

Based on the calculated values, it is possible to observe that the change in the metallic precursor does not significantly influence the
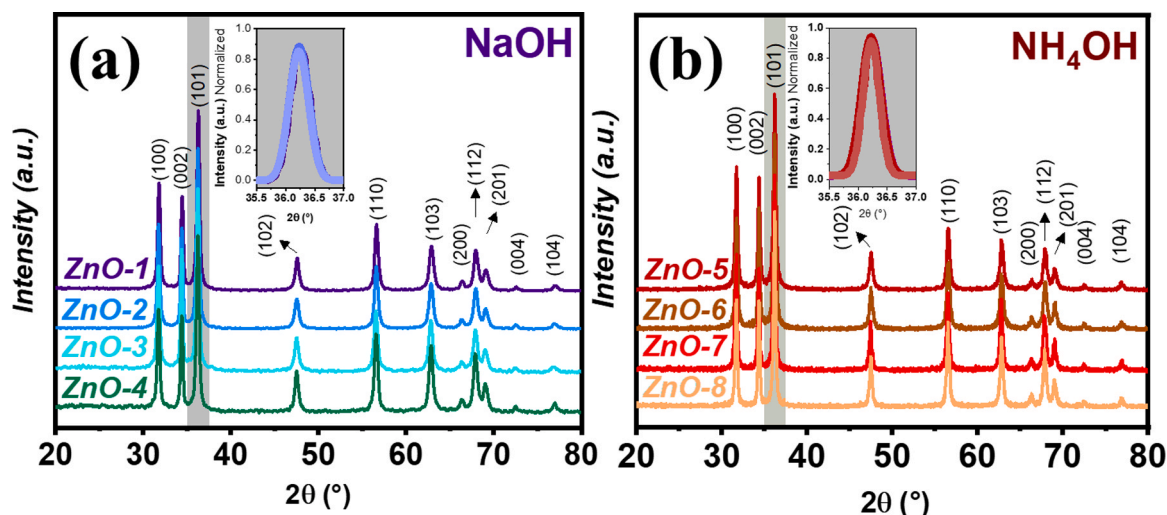
Fig. 1. XRD patterns of samples obtained using (a) NaOH and (b) NH$_4$OH.

Table 2
Minimal inhibitory concentration of ZnO NPs and daptomycin against gram-positive bacteria.

Bacterial strains	MIC (mg/L)					
	ZnO 1	ZnO 2	ZnO 3	ZnO 4	ZnO 7	Dap
S. epidermidis ATCC 35984	512	512	256	256	512	< 0.125
S. aureus ATCC 25923	> 512	512	512	256	512	0.5
S. aureus ATCC 8095	> 512	> 512	512	512	> 512	1
E. faecium ATCC 700221	512	512	512	> 512	512	1

Dap – Daptomycin

values of the two network parameters, *a* and *c*. This similarity corroborates the heights of the two diffraction peaks corresponding to the plane (101), which also did not present differences in both groups of samples (insert Fig. 1a-b). This result agrees with Gatou et al., which investigated the effect of zinc acetate, nitrate, chloride, or sulfate on the preparation of ZnO-NPs [47]. The degree of distortion of the unit cell (R) was also calculated from values of a and c substituted in Eq. (1), in which values of R = 1 are attributed to a distortion-free unit cell [48].

$$R = \frac{\left(2a\sqrt{\frac{2}{3}}\right)}{c} \tag{1}$$

The *R* values presented in Table S1 confirm that the synthesis methods applied in this study efficiently produce ZnO with high crystallinity and without distortion in the unit cells, regardless of the variable used (Table 3). With the similarity of the structural characterization results of the ZnO samples, the inhibitory selectivity of the ZnO NPs against gram-positive bacteria can be related to the surface interactions.

This is because there are different interactions at the solid-liquid interface (nanoparticles-test medium) and the solid-liquid contact zone with biological groups (bacteria). These interactions depend on the polarity of the crystalline facets of the ZnO NPs and the characteristics of the cell membranes of the studied bacteria [49].

The plane (101) corresponding to the facet of semi-polar nature showed the highest peak intensity in the XRD analyses (Fig. 1). This plane is characterized by presenting an angle of ~ 45º about the eixo-*c* (axial) in the 3D ZnO structures contributing to the formation of pointed shapes in the axial or oval direction when combined with axial growth in the (100) plane [50]. The morphological characteristics of nanomaterials were evaluated from the type of base solution (NaOH or NH$_4$OH), Zn^{2+} [Zn (NO$_3$)$_2$ or Zn (CH$_3$COO)$_2$] precursor, and reaction time (15 or 30 min). In NaOH solution, Fig. 2a shows that using the Zn (NO$_3$)$_2$ precursor and 15 min synthesis time, spherical particles (Insert-Fig. 2a) with an average diameter of 44.17 ± 17.13 nm are obtained as agglomerates. Increasing the synthesis time up to 30 min, particles increase in 30% their average diameter (57.59 nm ± 17.00 nm) with preferential growth in the radial direction (100), (101), and moderate in the axial direction (002) until obtaining the oval form [51]. Still in NaOH solution, when applying Zn(CH$_3$COO)$_2$ as a precursor of Zn^{2+}, nanorods with an average diameter of 74.59 ± 27.45 nm and face (002) with reduced diameter in the radial direction are produced in 15 min of synthesis (Fig. 2c). Increasing time to 30 min, the amount of nanorods decreases, and a mixture of spherical particles, and rods are observed, possibly due to the dissolution of the rods and re-precipitation in an oval shape (Fig. 2d).

To understand the influence of the metallic precursor on the morphology of the particles, the reactions from 2 to 4 describe the formation of ZnO in a basic medium [52].
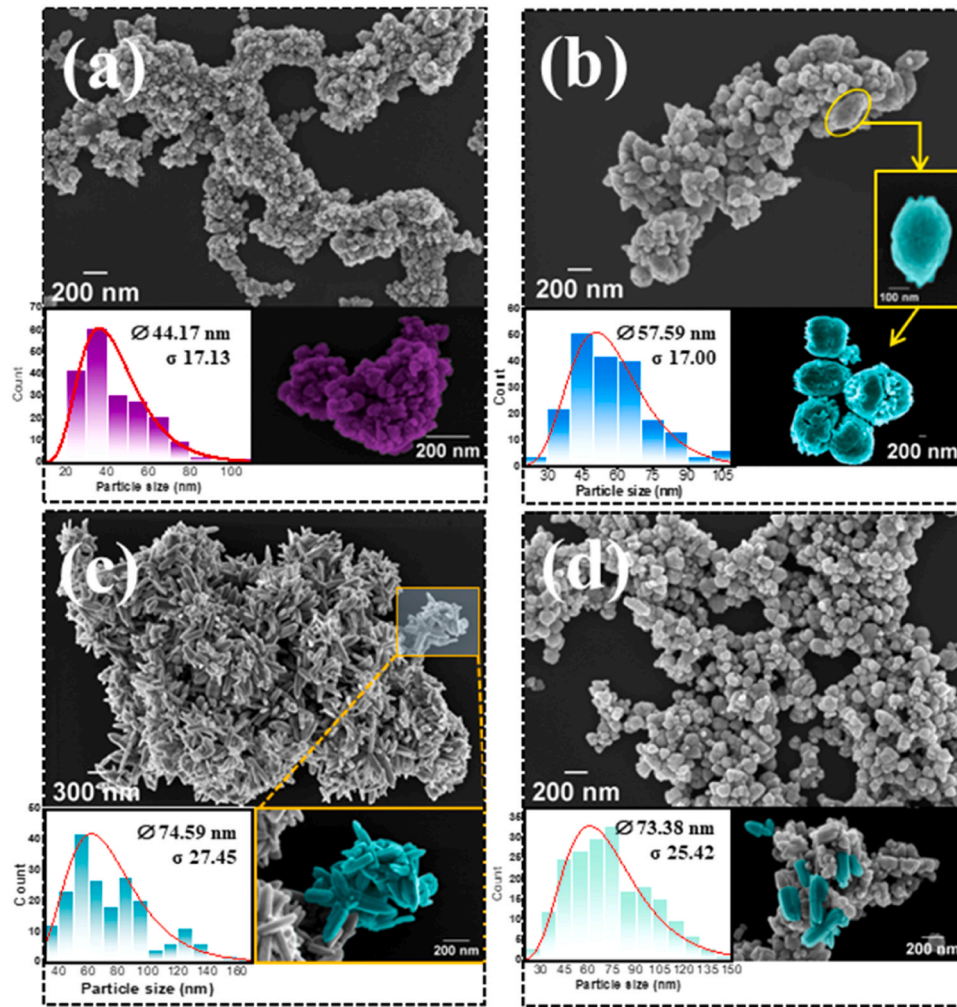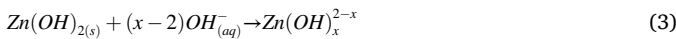
$$Zn^{2+}_{(aq)} + 2OH^{-}_{(aq)} \rightarrow Zn(OH)_{2(s)} \tag{2}$$

Table 3
Rietveld refinement parameters and ZnO unit-cells.

Sample	a=b (Å)	c (Å)	c/a (Å)	Volume (Å^3)	Density	x^2	Crystallite size (nm)
ZnO-1	3.2490 (5)	5.2073 (5)	1.6027	47.605 (3)	5.683 (3)	2.15	18.43 ± 3.22
ZnO-2	3.2499 (5)	5.2084 (5)	1.6026	47.644 (3)	5.723 (3)	2.23	18.50 ± 3.40
ZnO-3	3.2499 (5)	5.2088 (5)	1.6027	47.646 (3)	5.706 (3)	2.06	19.33 ± 3.23
ZnO-4	3.2499 (5)	5.2087 (5)	1.6027	47.645 (3)	5.708 (3)	2.00	18.51 ± 3.41
ZnO-5	3.2534 (5)	5.2134 (5)	1.6027	47.792 (3)	5.586 (3)	1.34	18.83 ± 3.40
ZnO-6	3.2491 (5)	5.2074 (5)	1.6027	47.608 (3)	5.708 (3)	2.05	18.66 ± 3.02
ZnO-7	3.2499 (5)	5.2087 (5)	1.6027	47.644 (3)	5.700 (3)	2.06	21.65 ± 2.77
ZnO-8	3.2510 (5)	5.2105 (5)	1.6027	47.695 (3)	5.675 (3)	2.04	22.24 ± 4.19

Fig. 2. SEM micrographs of (a) ZnO-1, (b) ZnO-2, (c) ZnO-3, and (d) ZnO-4 prepared in an alkaline medium using NaOH.

$$Zn(OH)_{2(s)} + (x-2)OH^-_{(aq)} \rightarrow Zn(OH)^{2-x}_x \qquad (3)$$

$$Zn(OH)^{2-x}_x \rightarrow ZnO + H_2O + (x-2)OH^- \qquad (4)$$

As can be seen in Eqs. (2)–(4), the anions NO_3^- and CH_3COO^- do not participate directly in the precipitation of Zn^{2+} in the form of ZnO. However, when crystallization nuclei are formed, the polar facets (002) alternate between negative (O^{2-}) and positive (Zn^{2+}) due to the O-Zn-O bonds increasing in the axial direction [53]. Thus, the non-polar facets (101), (002) interact with the NO_3^- or CH_3COO^- anions when the O-polar characteristics assume the axial growth plane [54]. Considering that the acetate ion has a less polar character than NO_3^-, this is preferentially deposited on the non-polar facet of ZnO. On the other hand, $Zn(OH)_4^{2-}$ and NO_3^- compete for deposition on the Zn-polar facet. When the O-polar facet takes over the growth face, $Zn(OH)_4^{2-}$ can deposit on the non-polar face in competition with the acetate ion. This behavior results in radial and ax; however, in the presence of an acetate ion, axial growth is preferable more significantly greater interaction than the acetate ion presents with the non-polar face [55]. In addition, $Zn^{2+}_{(aq)}$ or $Zn(OH)_2,$ formed in NaOH solution, interact with the non-polar face (101), (002), increasing the diameter in the radial direction, which produces spherical-shaped particles. As the reaction time increases, the adsorption-desorption equilibrium exposes all facets, resulting in more significant interaction in these positions. Consequently, moderate ZnO precipitation in the axial direction is achieved within 30 min to obtain a surface that tends to smaller diameters (tape) [56]. Unlike the NaOH solution, using NH_4OH can form other complexes with Zn^{2+}. Thus, the morphological characteristics of nanomaterials when using an NH_4OH solution in the presence of precursors $Zn(NO_3)_2$ or $Zn(CH_3COO)_2$ after 15 or 30 min of reaction are shown in Fig. 3.

In addition to the $[Zn(OH)_4]^{2-}$ complex and $Zn(OH)_2$ formed in the presence of hydroxyls, the dissolved ammonia when the base used is NH_4OH produces the complex $[Zn(NH_3)_4]^{2+}$ (Eq. 5) [57].

$$Zn^{2+}_{(aq)} + 4NH_{3(aq)} \leftrightarrows [Zn(NH_3)_4]^{2+} \qquad (5)$$

Then, the $[Zn(NH_3)_4]^{2+}$ complex reacts with excess hydroxyls, releasing ammonia to convert to the $[Zn(OH)_4]^{2-}$ complex, as shown in Eq. (6).

$$[Zn(NH_3)_4]^{2+}{}_{(aq)} + 4OH^-{}_{(aq)} \leftrightarrows [Zn(OH)_4]^{2-}{}_{(aq)} + 4NH_{3(aq)} \qquad (6)$$
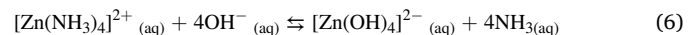
In the last step, the reaction proceeds as described in Eq. (7), and ZnO is finally formed [57].

$$Zn(OH)_2(s) + [Zn(OH)_4]^{2-} (aq) \rightarrow \Delta\ 2ZnO(s) + 2\ H_2O_{(l)} + 2OH^- (aq) \quad (7)$$
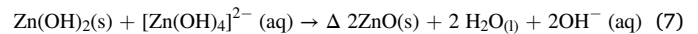
The chemical composition of non-reacting Zn^{2+} species is more complex in the presence of NH_4OH compared to NaOH. In NH_4OH solution, Zn^{2+} appears as $Zn^{2+}_{(aq)}$, $Zn(OH)_{2(s)}$, $[Zn(OH)_4]^{2-}_{(aq)}$ and $[Zn(NH_3)_4]^{2+}_{(aq)}$. As a crystallization nucleus is formed, electrostatic interaction can occur in all facets due to the different polarities of the Zn^{2+} intermediates. When the $Zn(NO_3)_2$ precursor is used, the NO_3^- ion interacts with the polar-Zn facet and inhibits axial growth. However, the interaction of the polar-Zn facet with $[Zn(OH)_4]^{2-}$ can also occur
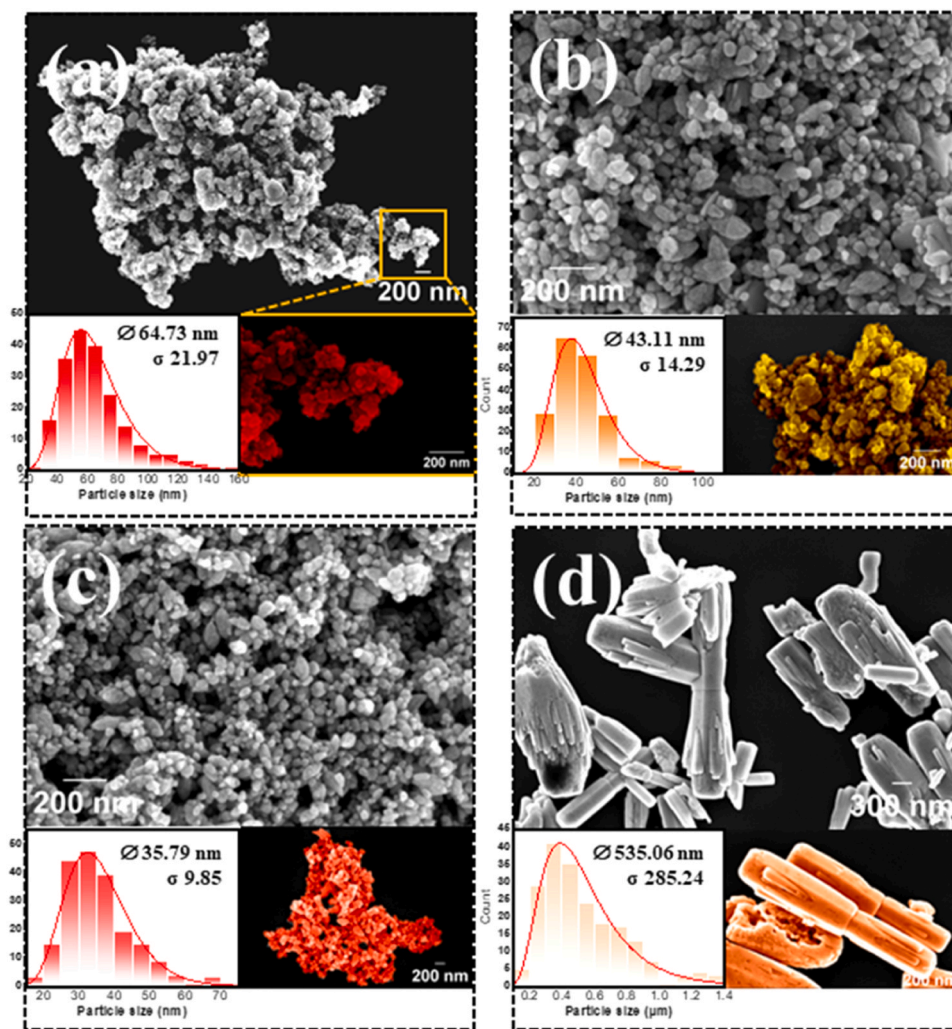
Fig. 3. SEM micrographs of (a) ZnO-5, (b) ZnO-6, (c) ZnO-7, and (d) ZnO-8 prepared in an alkaline medium using NH$_4$OH.

moderately since the mobility of $[Zn(OH)_4]^{2-}$ is lower compared to NO$_3$ [58]. Furthermore, positively charged Zn^{2+} species can interact with the O-polar face and grow in the axial direction. However, the adsorption energy of the O-polar facet is unfavorable, and the smaller number of interaction sites limits growth in this direction [59]. Thus, the interactions of the O-polar facet can be enhanced in the presence of $[Zn(NH_3)_4]^{2+}$, distributing axial growth with the Zn-polar facet, forming rod structures. At the same time, Zn(OH)$_2$ can precipitate in the non-polar facet and increase in diameter in the radial direction. In general, the complex composition of the system allows growth in all directions, with a greater tendency towards the radial direction due to the saturation of the Zn-polar face by NO$_3^-$ ions at any reaction time.

In the presence of the zinc acetate precursor, the non-polar facets are restricted by the more efficient adsorption of the acetate ions, resulting in preferential growth in the axial direction. This tendency increases with reaction time, which is evidenced by the more significant number of rods observed in Fig. 3d. FTIR analyses showed that for the ZnO-3, ZnO-4, and ZnO-8 samples, peaks centered at 1405 and 1550 cm^{-1}, especially, were more intense (Fig. S10). These peaks are attributed to the presence of acetate ions of the Zn-precursor [60], which were adsorbed with greater efficiency on the non-polar facets, contributing to the axial growth and formation of rods in these samples. Therefore, the ZnO-5 sample mostly showed the presence of nanospheres, and, in some regions of the image, it was possible to observe the presence of particles with the shape of a straight hexagonal prism with a central cavity (insert of Fig. 3a). Particle size was also affected by the microwave oven

treatment time when the histograms of Fig. 3a-b are compared for samples ZnO-5 and ZnO-6. Nanospheres formed in sample ZnO-5 have an average length of 64.73 nm ($\pm$ 21.97 nm), while in piece ZnO-6 was 43.11 ($\pm$ 14.29). The EDX of ZnO NPs reveals the presence of Zn and O, which confirms the synthesis of pure ZnO nanoparticles (Fig. S11 - Supplementary Material).

Crystallite size is a structural parameter associated with preferential growth in NPs, and their size can be significantly dependent on the synthesis conditions [61]. Therefore, we chose it as a response to analyze the effect of metallic precursor, base type, and MW irradiation time on ZnO synthesis. Thus, the percentage of each effect on the crystallite size and your cumulative sum have been calculated to evaluate the strategies that have a significant effect (Fig. 4a).

The base (effect B) and the MW irradiation time (effect C) were the most relevant effects on the crystallite size. The metallic precursor (effect A) contributed less than 1% to the response and the remaining secondary and tertiary effects. Fig. 4b illustrates the effects' magnitude, direction, and significance. The negligible effects conform to a normal distribution with a zero mean on the x-axis, according to the fit line (red). The significant effects exhibit nonzero means and are more distant from the red straight line. The positive estimated effect B revealed that the crystallite size increased with increasing B at the studied levels. This is because in the presence of NH$_4$OH (upper B level), the different complex structures of Zn^{2+} interact with more ZnO facets, promoting an increase in crystallite size. The variable C has also shown a significant effect on the system; increasing the crystallite size when it is increased
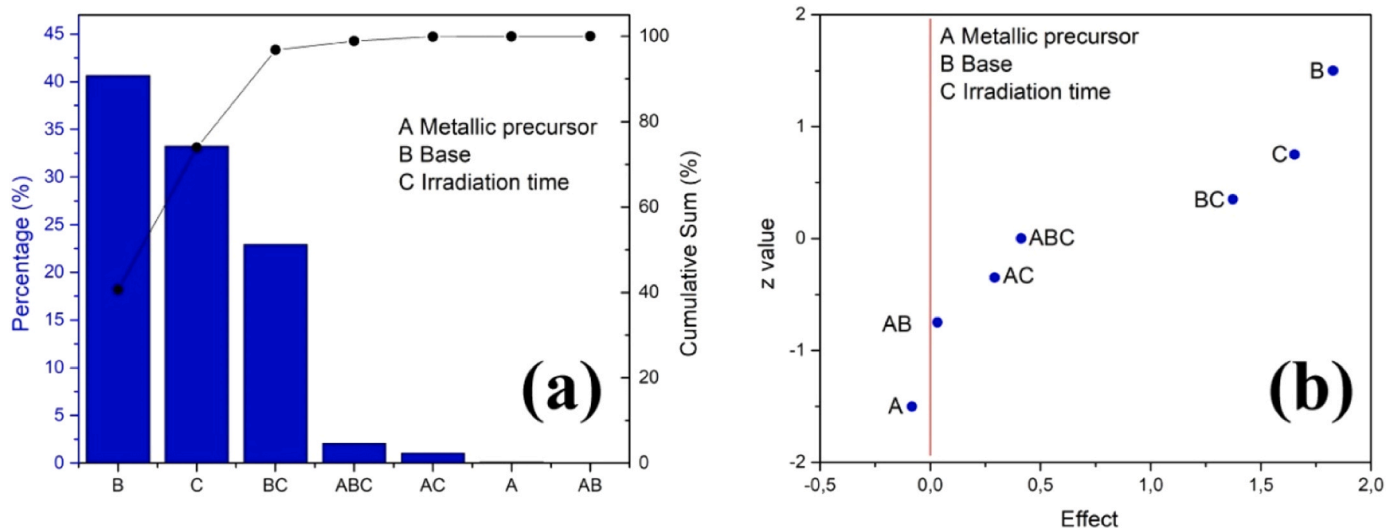
Fig. 4. (a) Percentage of each effect on the crystallite size (μm) and cumulative sum and (b) the probability graph of effects.

due to the longer interaction time of the ions on the ZnO facets. The negative estimated effect A reveals that the change in metallic precursor type is related to the decrease in crystallite size. The mechanisms of ZnO formation associated with the presence of A, B, and C are detailed below.

The preferential growth associated with the facets [(100), (002), and (101)] proved to be an essential factor in obtaining different morphologies. As their polarities improve interaction with the bacterial cell wall, the intensity of the 3 principal peaks [(100), (002), and (101)] was normalized by the highest intensity peak (101), and the ratio I(100)/I(002) was calculated [62]. All the calculated values of $I_{(100)}/I_{(002)} > 1$ confirm that the non-polar (100) and semi-polar (101) facets compose the majority of the ZnO nanostructures. The selective toxicity of ZnO-NPs against gram-positive bacteria is explained by the more significant electrostatic interaction that the non-polar facets (100, 101) show with the exposed peptidoglycan layer in this group of bacteria [63, 64]. Pranjali et al. [65] suggested that ZnO-NPs can interact and adsorb biological fluids, such as proteins, lipids, and metabolites, which could hinder the stability and reduce the antibacterial action of this [66]. Furthermore, zeta potential analyses (Fig. 5a) showed negative surface charges due to hydroxyl or acetate on the surface of ZnO-NPs.

The acetate and hydroxyl groups on the ZnO-NPs surface can easily link with the amine or hydroxyl groups of peptidoglycans to increase bacteria exposure to ZnO-NPs [67]. In this way, when the electrostatic interaction (ZnO-NPs/Gram-positive bacteria) occurs, in addition to the

damage caused to the peptidoglycan layer, the Zn^{2+} ions dissolved in the solution or present in the polar facet (001) more easily reach the cell cytoplasm [68]. Only ZnO-7 showed a positive surface charge, which can be attributed to the more significant amount of Zn^{2+} ions on the surface of this material (Fig. 5b).

As Zn^{2+} ions are also highly toxic to bacteria, their bactericidal activity is also noted. The inactivity observed for Gram-negative bacteria is due to the thinner and more complex cell wall, composed of an outer layer of lipopolysaccharides that can act as a protective shield against damage to the surface and, consequently, override the inactivation mechanisms [67,69–73]. Fig. 5c shows the characteristic structures of the bacterial membrane. Other results of the antibacterial activity of ZnO-NPs are reported in the literature [74,75]. Considering the properties of ZnO NPs discussed above, the samples that exhibited antibacterial activity, namely ZnO-1, ZnO-2, ZnO-3, ZnO-4, and ZnO-7, were chosen for determining the MIC followed by the PCA analysis.

3.2. Minimum inhibitory concentration and PCA analysis

The objective was to apply the MIC values in conjunction with PCA to evaluate the metabolic response of bacterial strains after treatment with ZnO antibacterial materials. By transforming MIC values into a reduced set of uncorrelated components, PCA reveals hidden relationships and trends that might be obscured in the original high-dimensional data. The plot of the PCAs discrimination functions with the MIC values (Fig. 6) revealed a degree of segregation between the classes, meaning that the methodology allowed for detecting variables that differentiate antimicrobial agent groups. PCA eigenvalues indicate that the first two axes explain 94.6% of the total variability (PC1 explains 85.5% and PC2 9.1%). Therefore, these two PCs were selected for further analysis and visualization. The contribution of each variable, their relationships, and the resulting principal components were illustrated in Fig. 6. The PC1 exhibited a strong positive correlation with the ≤ 128 mg/mL concentrations, i.e., inhibition is not overly evidenced compared to controls. However, the antibacterial activity at 256 and 512 mg/mL concentrations showed a significant negative correlation with PC2, indicating that the bactericidal action is inhibited at these concentrations.

A few observations were made from the score plot for PC1 to PC2 for all treatments (Fig. 6), where the samples of bacterial strain pure and those treated with ZnO materials (ZnO-1, ZnO-2, ZnO-3, ZnO-4, and ZnO-7) are grouped. It is essential to notice that the PCAs models could distinguish well the samples of all non-treated bacterial strains, as a bacterial control group, from those exposed to one of the antibacterial agents. In one quadrant, the control samples are positioned as a distinct
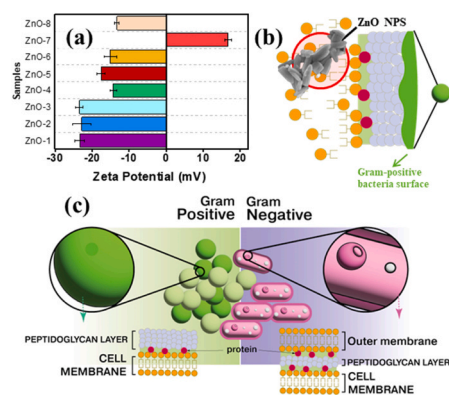

Fig. 5. (a) zeta potential values (b) illustration of the mechanism of damage to the surface of gram-positive bacteria (membrane disruption and cytoplasmic leakage) caused by electrostatic interaction between NPs and the microorganism and (c) characteristic structures of the bacterial membrane.
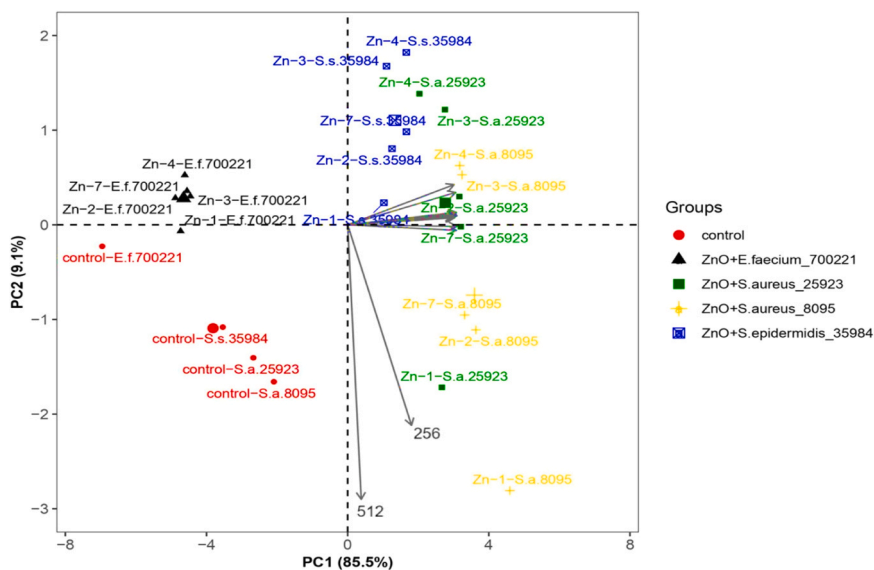
Fig. 6. PCA results: Projections of scores and loadings for the first two principal components.

cluster, markedly distant from other classes, displaying exclusively negative score values for both PCs. The bacterial strains (*S. aureus* ATCC 25923 and 8095, and *S. epidermidis* ATCC 35984) treated with ZnO materials in the upper right quadrant, e.g., ZnO-3 and ZnO-4, were compelling and inhibited bacterial growth. In contrast, materials on the low right quadrant, e.g., ZnO-1, ZnO-2, ZnO-3, and ZnO-7, were less effective. The *E. faecium* ATCC 700221 samples are mainly placed in a cluster on the upper left quadrant of the plot. Similarly, *E. faecium* ATCC 700221 samples treated with ZnO materials such as ZnO-3 and ZnO-4 effectively inhibit bacterial growth—conversely, other tests like ZnO-1, ZnO-2, ZnO-3, and ZnO-7are comparatively less effective.

This tendency could be associated with the mentioned nanoparticles' high antibacterial activity and structural differences. The different MIC values are due to the sensitivity by which other mechanisms can inactivate each type of Gram-positive bacteria. Our results showed that the possible tools are the direct interaction between material-bacteria in the non-polar facets, the presence of Zn^{2+} ions in the solution, and especially ROS. For the latter, the production of ROS by the ZnO-NPs is an essential mechanism for inhibited bacterial activity since these can be produced even without light [76,77]. The formation of ROS (OH$^\bullet$, H_2O_2, $O_2^{\bullet-}$ and $^\bullet O_2$) and the interaction of these species with DNA, proteins, and enzymes can lead to the deregulation of vital processes for the cellular maintenance of these microorganisms. Among the ROS species with the most significant potential to cause oxidative stress, the hydroxyl radical (OH$^\bullet$) can react with virtually all constituents present in bacteria. Its first targets are proteins, DNA, and lipids, which can form other secondary ROS from the interaction and reaction [78]. As the formation of ROS is enhanced under light, photocatalytic studies have been carried out.

3.3. Photocatalytic and cytotoxic activity

From diffuse reflectance measurements, the bandgap energy (E_{gap}) of the ZnO samples was calculated using the Tauc equation (Table 4, Fig. S15) [79]. The E_{gap} values varied from 3.09 to 3.12 eV, and considering all the samples, an $E_{gap(mean)} = 3.11 \pm 0.01$ eV was obtained. The results reveal that the absorption of light energy does not show significant variation for the different samples and that the photocatalytic activity is expected for $\lambda < 401$ nm, corresponding to the region of transition of ultraviolet-visible absorption. Therefore, the photodegradation assays of MB under UV light confirmed the photocatalytic activity of materials for the dye degradation (Figs. S16 and

Table 4
Band gap values of ZnO-NPs samples, BET surface area, percentage of MB removal after photocatalysis tests using a UV lamp, and kinetic data.

Sample	Band gap (eV)	BET Surface Area (m^2/g)	Maximum removal (%)	k x 10^{-3} min^{-1}/R^2
Photolysis	–	–	6	0.76 / 0.443
ZnO − 1	3.12	19.106	75	22.9 / 0.955
ZnO − 2	3.10	10.163	40	8.05 / 0.955
ZnO − 3	3.09	3.846	67	17.6 / 0.992
ZnO − 4	3.11	10.020	72	22.3 / 0.983
ZnO − 5	3.11	2.116	75	24.1 / 0.980
ZnO − 6	3.11	16.098	8	1.24 / 0.945
ZnO − 7	3.12	18.385	50	11.4 / 0.991
ZnO − 8	3.12	1.000	57	13.7 / 0.937

S17), except ZnO-6, which reached a very low efficiency ($<10\%$) and was comparable to photolysis (Table 4).

For the other materials, the photocatalytic efficiency was at least 75% in 60 min, which represents a significant increase when compared to the photolysis and ZnO-6 (Fig. 7a). The pseudo-first-order kinetic constants were calculated and displayed in Table 4 together with the respective linear correlation coefficients (R^2). The values of $R^2 > 0.9$ for the photocatalytic tests show an excellent adjustment to the kinetic model attributed, evidencing a better performance for the samples that tend to form rods with smaller average diameters. In addition, the improved photocatalytic process observed for the ZnO-1 and ZnO-4 samples (Table 4) may be related to the increased surface area and, consequently, the more significant number of reactive sites available for charge transfer. The literature shows that using ZnO as a photocatalyst has some limitations due to the recombination processes of the photogenerated charge carriers, and the low photocatalytic activity of the ZnO-6 sample can be attributed to this factor [80]. On the other hand, the high efficiency and higher kinetic constants obtained for ZnO-1, ZnO-3, ZnO-4, and ZnO-5 allow us to conclude that the recombination processes are not very significant in these samples. Therefore, the photocatalytic mechanism was studied in detail using reactive oxygen species (ROS) scavengers, selecting as reference the sample ZnO-5 that achieved optimal removal and the highest value of *k* in the MB photodegradation assays. The results shown in Fig. 7b confirm a reduction in photocatalytic efficiency when MeOH and TBA are used as $^\bullet$OH and h$^+$ scavengers, respectively. The contribution of h^+ and $^\bullet OH$ to the photochemistry mechanism directly correlates with each other and shows that
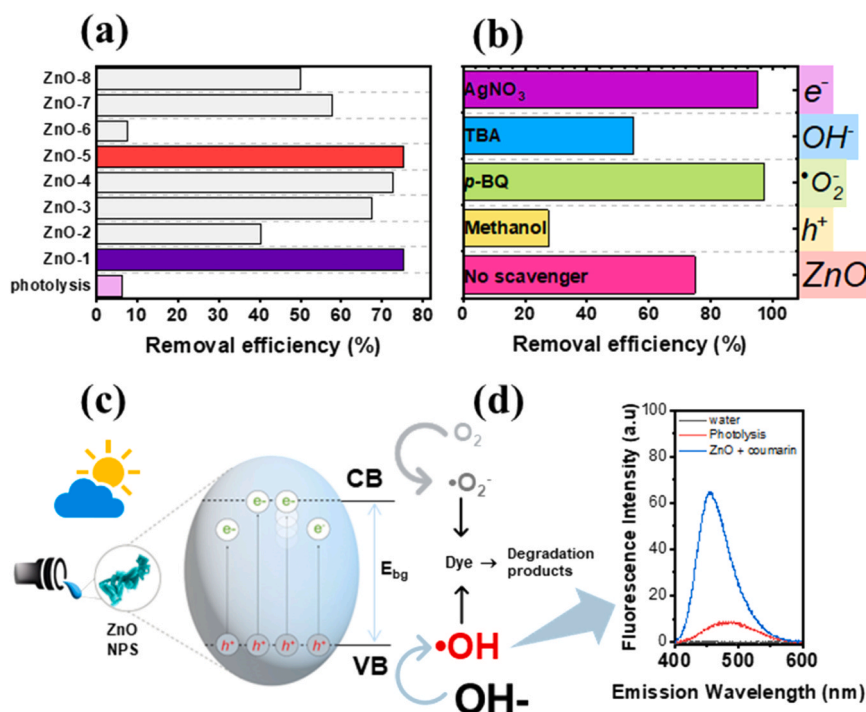
Fig. 7. (a) Efficiency of the MB photodegradation process using different ZnO NPs samples, (b) scavenger tests for determination of reactive oxygen species (ROS) using the ZnO – 5 sample, (c) proposed photodegradation mechanism and (d) fluorescence spectra of OH generation using coumarin (λ exc = 332 nm).

the optimal photocatalytic response of materials occurs in the oxidation sites. However, removal efficiency was increased in the presence of $AgNO_3$ and p-BQ compared to pure photocatalysts. These results show that the electrons photogenerated and available in the BC are easily transferred to the respective electron acceptors, maintaining the flow of formation of h^+ and consequent oxidation of water to produce the $^\bullet OH$. Thus, in the absence of electron acceptors, the formation of $O_2^{\bullet-}$ cannot be ruled out even if its activity is insignificant compared to the h^+ and $^\bullet OH$ in the degradation mechanism (Fig. 7c).

In summary, when ZnO is stimulated by light, the VB electrons are excited to BC. The photogenerated holes are active to oxidize water into hydroxyl radicals, which were verified in this study using the coumarin probe assay and shown in Fig. 7d. In this test, when $^\bullet OH$ is formed, it reacts with coumarin and forms umbelliferone, which exhibits an emission peak centered at 453 nm when excited with λ = 332 nm [81]. In sequence, the photo-excited electrons for CB can reduce O_2 to $O_2^{\bullet-}$, as shown in Fig. 7c and the series of reactions described in Eqs. (8)–(12), promoting efficient oxidation of the organic pollutant.

$$ZnO\text{-}NPs + h\nu \rightarrow h^+(VB) + e^-(CB) \tag{8}$$

$$h^+(VB) + H_2O \rightarrow {}^\bullet OH + H^+ \tag{9}$$

$${}^\bullet OH + MB \rightarrow byproducts \tag{10}$$

$$e^-(CB) + O_2 \rightarrow O_2^{\bullet-} \tag{11}$$

$$O_2^{\bullet-} + MB \rightarrow byproducts \tag{12}$$

Zn^{2+} leaching after 60 min of photocatalysis was monitored by FAAS and reached values of $3.13 \pm 0.01\%$ (ZnO-1), $23.4 \pm 0.11\%$ (ZnO-2), $0.77 \pm 0.01\%$ (ZnO-3), $2.80 \pm 0.00\%$ (ZnO-4), $10.3 \pm 0.09\%$ (ZnO-5), $0.60 \pm 0.01\%$ (ZnO-6), $4.28 \pm 0.01\%$ (ZnO-7) and $1.33 \pm 0.01\%$ (Zn)$-$8). Except for the ZnO-2 and ZnO-5 samples, the leaching was insignificant, confirming that the Zn^{2+} was crystallized in the form of ZnO with high efficiency. However, the highest leaching values observed for the ZnO-2 and ZnO-5 samples indicate the presence of Zn^{2+} ions adsorbed on the materials' surface, which migrate easily into the solution. As the literature reports that Zn^{2+} ions are excellent bactericidal

agents, in addition to the evidenced photocatalytic activity, the bactericidal activity of the materials can be obtained. The excellent performance of the ZnO NPs obtained in this study was compared to other works in the literature under approximate application conditions (Table 5). After comparison, it is evident that ZnO-5 is a competitive photocatalyst for oxidation studies of organic pollutants, which added to the optimal results of bactericidal activity discussed above, confirming its versatility.

In addition to considering the toxic effects of ZnO NPs against microorganisms of global interest, it is also essential to understand these materials' effects on plants, as these are considered critical components of ecosystems [87]. This is even more important because some studies have demonstrated the possibility of translocation and subsequent bioaccumulation process of the NPs from their contact with the soil and their displacement to the plants from the roots [87–89]. The phytotoxicity tests investigated here were based on the seed germination rate and root growth of C. sativus due to the high germination rate and rapid root growth time of this species [90,91]. Evaluating these two parameters represents a fast and effective method to test phytotoxicity, presenting several advantages, such as sensitivity, simplicity, and low cost [43]. The germination rate values of *C. sativus* seeds did not vary as significantly compared to the control sample (Fig. 8a-b). Despite this, samples ZnO-1, ZnO-2, and ZnO-7 presented, respectively, a growth rate around 90%, 80% and 90% (Fig. 8a). This behavior can be attributed to the smaller particle size of these samples (44.17, 57.59, and 35.79 nm, respectively), which facilitated the penetration process of the NPs into the seeds. Zhang et al. [87] also observed a lower effect of ZnO NPs on the germination rate of *C. sativus* seeds. They attributed these results to some sensitive factors that need further investigation, such as the low concentration of the NPs used in the tests for accurate toxicity determination and the short exposure time.

Regarding root length, it can be observed that all treatments with the ZnO-NPs affected root growth resulting in rates of less than 10% (Fig. 8b). This reduction in root size of *C. sativus* may be mainly associated with the high release rate of Zn^{2+} ions due to dissolution of ZnO NPs, as was discussed by Zhang et, al who found no NPs per TEM even at

Table 5

Properties of ZnO photocatalysts produced under different conditions for MB degradation.

Catalyst characteristic	MB (mg/L) and photocatalyst dose (g/L)	Bandgap (eV) and Irradiation type	Removal efficiency (%) and time	Size and shape of NPs	Ref
ZnO biosynthesized using the seed extract of *Moringa oleifera*	50, 20	[a] UV irradiation (k360 nm)	71 in 24 h	28 nm, spherical	[82]
ZnO biosynthesized using different amounts of *Camellia sinensis* extract	15 1	[a] UV irradiation	84 in 120 min	8 nm, rounded particles	[83]
ZnO synthesized using precipitation and sol-gel method	20 0.25	3.44 and 3.35 UV lamp (Philips, 12 W)	81.02 e 92.48 in 180 min	[b]	[84]
ZnO	10 0.25	sunlight	95.30 in 70 min	5 nm, nano-flakes	[85]
ZnO synthesized using Tabernaemonana divaricate	10 1	3.26 Direct sunlight	~100 in 90 min	20 – 50 nm Spherical	[86]
ZnO synthesized by microwave-assisted hydrothermal method	20 1	~3.11 UV	75 in 60 min	Different morphologies	This work

*dye concentration not mentioned.

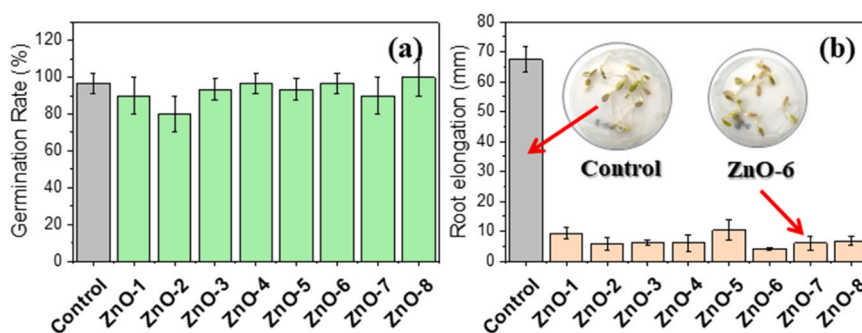[a] Bandgap not informed.

[b] Size and shape not informed.

Fig. 8. Effect of ZnO-NPs on (a) germination rate and (b) root growth of *C. sativus*.

relatively high concentration (1000 mg/L) [87]. Furthermore, the generation of ROS above the capacity of the detoxification mechanisms of the investigated species and the effect of the morphology of the NPs may directly impact plant development. Plant cell walls have pore sizes of up to 20 nm, making the entry of NPs within this size range possible.

4. Conclusion

ZnO NPs with different morphologies were easily obtained using the microwave-assisted hydrothermal method with varying zinc precursors. The physicochemical properties of ZnO NPs showed high crystallinity and a tendency to form non-polar and semi-polar facets in all samples. In the application step, high kinetic constant values ($k = 24.1 \times 10^{-3}$ $min^{-1}/R^2 = 0.980$) and removal rates of 75% in 60 min for MB pollutants were achieved. This efficiency was due to the photocatalytic mechanism of the formation of ROS, especially hydroxyl radicals. As an essential technological application of ZnO NPs, the bactericidal activity of the materials showed high selectivity to inactivate highly resistant Gram-positive bacteria. The PCA results confirm that two key components can explain the MIC values for various groups of bacteria and materials. Among these, the MIC values of 256 and 512 mg/mL are the only ones displaying significance in inhibition rates. Notably, this significance is observed mainly for the ZnO-3 and ZnO-4 materials, which effectively inhibit the bacterial growth of all four gram-positive bacteria evaluated in this study. Phytotoxicity assays also showed changes in plant cells in the presence of ZnO NPs, and this behavior is due to the formation of ROS and Zn^{2+} ions from nanomaterials. Therefore, materials with high photocatalytic activity and inhibition of resistant bacteria were quickly produced. These ZnO NPs can be natural alternatives to obtain new technologies applied to the chemical treatment and bacteriological inactivation of contaminated water.

CRediT authorship contribution statement

Marques Gleison Neres: Conceptualization, Data curation, Formal analysis, Investigation, Methodology, Project administration, Resources, Software, Supervision, Validation, Visualization, Writing – original draft, Writing – review & editing. **Moreira Ailton José:** Conceptualization, Data curation, Formal analysis, Investigation, Methodology, Project administration, Validation, Visualization, Writing – original draft, Writing – review & editing. **Nobrega Eryka Thamyris Damascena:** Conceptualization, Data curation, Formal analysis, Software, Writing – original draft, Writing – review & editing. **Braga Sandalene:** Conceptualization, Data curation, Investigation, Methodology, Project administration. **Argentin Marcela Nunes:** Conceptualization, Data curation, Formal analysis, Investigation, Methodology, Writing – original draft, Writing – review & editing. **Camargo Ilana Lopes Baratella da Cunha:** Conceptualization, Project administration, Resources, Writing – original draft, Writing – review & editing. **Azevedo Emilio:** Conceptualization, Data curation, Resources. **Pereira Ernesto:** Data curation, Funding acquisition, Supervision, Validation, Visualization, Writing – original draft, Writing – review & editing. **Basso Bernardi Maria Inês:** Conceptualization, Data curation, Formal analysis, Funding acquisition, Methodology, Project administration, Resources, Supervision, Validation, Visualization, Writing – original draft, Writing – review & editing. **Mascaro Lucia Helena:** Conceptualization, Data curation, Funding acquisition, Methodology, Project administration, Resources, Supervision, Validation, Visualization, Writing – original draft, Writing – review & editing.

Declaration of Competing Interest

The authors declare that they have no known competing financial interests or personal relationships that could have appeared to influence

the work reported in this paper.

Data Availability

Data will be made available on request.

Acknowledgments

Appendix A. Supporting information

Supplementary data associated with this article can be found in the online version at doi:10.1016/j.jece.2023.111870.

References

[1] S. Bungau, D.M. Tit, T. Behl, L. Aleya, D.C. Zaha, Aspects of excessive antibiotic consumption and environmental influences correlated with the occurrence of resistance to antimicrobial agents, Curr. Opin. Environ. Sci. Health 19 (2021) 100224, https://doi.org/10.1016/j.coesh.2020.10.012.

[2] L.B. Rice, Federal funding for the study of antimicrobial resistance in nosocomial pathogens: no ESKAPE, J. Infect. Dis. 197 (2008) 1079–1081, https://doi.org/10.1086/533452.

[3] D.M.P. De Oliveira, B.M. Forde, T.J. Kidd, P.N.A. Harris, M.A. Schembri, S.A. Beatson, D.L. Paterson, M.J. Walker, Antimicrobial resistance in ESKAPE pathogens, Clin. Microbiol. Rev. 33 (2020), https://doi.org/10.1128/CMR.00181-19.

[4] F. Edwards, A. MacGowan, E. Macnaughton, Antibiotic resistance, Medicine 49 (2021) 632–637, https://doi.org/10.1016/j.mpmed.2021.07.006.

[5] M. Miretti, R. Clementi, T.C. Tempesti, M.T. Baumgartner, Photodynamic inactivation of multiresistant bacteria (KPC) using zinc(II)phthalocyanines, Bioorg. Med. Chem. Lett. 27 (2017) 4341–4344, https://doi.org/10.1016/j.bmcl.2017.08.028.

[6] L.V. Perdigão Neto, M.S. Oliveira, T.D. Orsi, G.V.B. do Prado, R.C.R. Martins, G. C. Leite, A.P. Marchi, E.S. de Lira, M.F. Côrtes, E.P.S. Espinoza, C.M.D. de M. Carrilho, Í. Boszczowski, T. Guimarães, S.F. Costa, A.S. Levin, Alternative drugs against multiresistant Gram-negative bacteria, J. Glob. Antimicrob. Resist 23 (2020) 33–37, https://doi.org/10.1016/j.jgar.2020.07.025.

[7] H. Yang, Q. Zhang, Y. Chen, Y. He, F. Yang, Z. Lu, Microwave–ultrasonic synergistically assisted synthesis of ZnO coated cotton fabrics with an enhanced antibacterial activity and stability, ACS Appl. Bio Mater. 1 (2018) 340–346, https://doi.org/10.1021/acsabm.8b00086.

[8] M. Assis, L.K. Ribeiro, M.O. Gonçalves, L.H. Staffa, R.S. Paiva, L.R. Lima, D. Coelho, L.F. Almeida, L.N. Moraes, I.L.V. Rosa, L.H. Mascaro, R.M.T. Grotto, C.P. Sousa, J. Andrés, E. Longo, S.A. Cruz, Polypropylene modified with Ag-based semiconductors as a potential material against SARS-CoV-2 and other pathogens, ACS Appl. Polym. Mater. 4 (2022) 7102–7114, https://doi.org/10.1021/acsapm.2c00744.

[9] G.C. Tremiliosi, L.P. Gustavo Simoes, D.T. Minozzi, R.I. Santos, D.C.B. Vilela, E. Luiz Durigon, R. Rahal Guaragna Machado, D. Sales Medina, L. Kelly Ribeiro, I. Lucia Viana Rosa, M. Assis, J. Andrés, E. Longo, L.H. Freitas-Junior, Ag nanoparticles-based antimicrobial polycotton fabrics to prevent the transmission and spread of SARS-CoV-2, (n.d.). https://doi.org/10.1101/2020.06.26.152520.

[10] N. Mahmud, M.I. Anik, M.K. Hossain, M.I. Khan, S. Uddin, M. Ashrafuzzaman, M. M. Rahaman, Advances in nanomaterial-based platforms to combat COVID-19: diagnostics, preventions, therapeutics, and vaccine developments, ACS Appl. Bio Mater. 5 (2022) 2431–2460, https://doi.org/10.1021/ACSABM.2C00123/ASSET/IMAGES/LARGE/MT2C00123_0015.JPEG.

[11] E. Sánchez-López, D. Gomes, G. Esteruelas, L. Bonilla, A.L. Lopez-Machado, R. Galindo, A. Cano, M. Espina, M. Ettcheto, A. Camins, A.M. Silva, A. Durazzo, A. Santini, M.L. Garcia, E.B. Souto, Metal-based nanoparticles as antimicrobial agents: an overview, Nanomaterials 10 (2020) 292, https://doi.org/10.3390/NANO10020292.

[12] A. Menichetti, A. Mavridi-Printezi, D. Mordini, M. Montalti, Effect of size, shape and surface functionalization on the antibacterial activity of silver nanoparticles, J. Funct. Biomater. 14 (2023) 244, https://doi.org/10.3390/JFB14050244.

[13] O. Choi, Z. Hu, Size dependent and reactive oxygen species related nanosilver toxicity to nitrifying bacteria, Environ. Sci. Technol. 42 (2008) 4583–4588, https://doi.org/10.1021/es703238h.

[14] C. Takahashi, T. Yamada, S. Yagi, T. Murai, S. Muto, Preparation of silver-decorated Soluplus® nanoparticles and antibacterial activity towards S.

[15] epidermidis biofilms as characterized by STEM-CL spectroscopy, Mater. Sci. Eng.: C 121 (2021) 111718, https://doi.org/10.1016/j.msec.2020.111718.

[15] C. Liao, Y. Li, S. Tjong, Bactericidal and cytotoxic properties of silver nanoparticles, Int. J. Mol. Sci. 20 (2019) 449, https://doi.org/10.3390/ijms20020449.

[16] B.S. Vasile, O. Oprea, G. Voicu, A. Ficai, E. Andronescu, A. Teodorescu, A. Holban, Synthesis and characterization of a novel controlled release zinc oxide/gentamicin–chitosan composite with potential applications in wounds care, Int. J. Pharm. 463 (2014) 161–169, https://doi.org/10.1016/j.ijpharm.2013.11.035.

[17] F. Shahmohammadi Jebel, H. Almasi, Morphological, physical, antimicrobial and release properties of ZnO nanoparticles-loaded bacterial cellulose films, Carbohydr. Polym. 149 (2016) 8–19, https://doi.org/10.1016/j.carbpol.2016.04.089.

[18] A. Al-Nabulsi, T. Osaili, A. Sawalha, A.N. Olaimat, B.A. Albiss, G. Mehyar, M. Ayyash, R. Holley, Antimicrobial activity of chitosan coating containing ZnO nanoparticles against E. coli O157:H7 on the surface of white brined cheese, Int. J. Food Microbiol. 334 (2020) 108838, https://doi.org/10.1016/j.ijfoodmicro.2020.108838.

[19] G.H. Attia, Y.S. Moemen, M. Youns, A.M. Ibrahim, R. Abdou, M.A. El Raey, Antiviral zinc oxide nanoparticles mediated by hesperidin and in silico comparison study between antiviral phenolics as anti-SARS-CoV-2, Colloids Surf. B Biointerfaces 203 (2021) 111724, https://doi.org/10.1016/j.colsurfb.2021.111724.

[20] M. Seray, A. Skender, A.S. Hadj-Hamou, Kinetics and mechanisms of Zn2+ release from antimicrobial food packaging based on poly (butylene adipate-co-terephthalate) and zinc oxide nanoparticles, Polym. Bull. 78 (2021) 1021–1040, https://doi.org/10.1007/S00289-020-03145-Z/TABLES/5.

[21] M.C. Uribe-López, M.C. Hidalgo-López, R. López-González, D.M. Frías-Márquez, G. Núñez-Nogueira, D. Hernández-Castillo, M.A. Alvarez-Lemus, Photocatalytic activity of ZnO nanoparticles and the role of the synthesis method on their physical and chemical properties, J. Photochem. Photobio. A Chem. 404 (2021) 112866, https://doi.org/10.1016/j.jphotochem.2020.112866.

[22] K. Sahu, S. Choudhary, J. Singh, S. Kuriakose, R. Singhal, S. Mohapatra, Facile wet chemical synthesis of ZnO nanosheets: effects of counter ions on the morphological, structural, optical and photocatalytic properties, Ceram. Int. 44 (2018) 23094–23101, https://doi.org/10.1016/j.ceramint.2018.09.116.

[23] J. Tang, J. Chai, J. Huang, L. Deng, X.S. Nguyen, L. Sun, T. Venkatesan, Z. Shen, C. B. Tay, S.J. Chua, ZnO nanorods with low intrinsic defects and high optical performance grown by facile microwave-assisted solution method, ACS Appl. Mater. Interfaces 7 (2015) 4737–4743, https://doi.org/10.1021/am508426z.

[24] K. Sahu, A.K. Kar, Counterion-induced tailoring of energy transfer in hydrothermally grown nanostructured ZnO for photocatalysis, Cryst. Growth Des. 21 (2021) 3656–3667, https://doi.org/10.1021/acs.cgd.0c01202.

[25] S. He, S. Zhang, J. Lu, Y. Zhao, J. Ma, M. Wei, D.G. Evans, X. Duan, Enhancement of visible light photocatalysis by grafting ZnO nanoplatelets with exposed (0001) facets onto a hierarchical substrate, Chem. Commun. 47 (2011) 10797, https://doi.org/10.1039/c1cc14360c.

[26] H. Pan, V.A. Risley, K.R. Martindale, M.D. Heagy, Photocatalytic reduction of bicarbonate to formic acid using hierarchical ZnO nanostructures, ACS Sustain Chem. Eng. 7 (2019) 1210–1219, https://doi.org/10.1021/acssuschemeng.8b04861.

[27] L.A. Gusmão, D.A. Peixoto, J.Z. Marinho, F.C. Romeiro, R.F. Gonçalves, E. Longo, C.A. de Oliveira, R.C. Lima, Alkali influence on ZnO and Ag-doped ZnO nanostructures formation using the microwave-assisted hydrothermal method for fungicidal inhibition, J. Phys. Chem. Solids 158 (2021) 110234, https://doi.org/10.1016/j.jpcs.2021.110234.

[28] S.C. Esparza González, E. Bolaina-Lorenzo, J.J. Pérez-Trujillo, B.A. Puente-Urbina, O. Rodríguez-Fernández, A. Fonseca-García, R. Betancourt-Galindo, Antibacterial and anticancer activity of ZnO with different morphologies: a comparative study, 3 Biotech. 11 (123AD) 68. ⟨https://doi.org/10.1007/s13205–020-02611–9⟩.

[29] X. Wang, L. Sø, R. Su, S. Wendt, P. Hald, A. Mamakhel, C. Yang, Y. Huang, B. B. Iversen, F. Besenbacher, The influence of crystallite size and crystallinity of anatase nanoparticles on the photo-degradation of phenol, J. Catal. 310 (2014) 100–108, https://doi.org/10.1016/j.jcat.2013.04.022.

[30] A. Biswas, U. Kar, N.R. Jana, Cytotoxicity of ZnO nanoparticles under dark conditions via oxygen vacancy dependent reactive oxygen species generation, Phys. Chem. Chem. Phys. 24 (2022) 13965–13975, https://doi.org/10.1039/D2CP00301E.

[31] A. Lipovsky, Z. Tzitrinovich, H. Friedmann, G. Applerot, A. Gedanken, R. Lubart, EPR study of visible light-induced ROS generation by nanoparticles of ZnO, J. Phys. Chem. C 113 (2009) 15997–16001, https://doi.org/10.1021/jp904864g.

[32] A.S. Sá, I.S. de Lima, L.M. Honório, M.B. Furtini, J.K.D. de Souza, F.E.P. dos Santos, H.M. Barreto, T.G. Tabuti, E.C. da Silva-Filho, E.R. Triboni, J.A. Osajima, ROS-mediated antibacterial response of ZnO and ZnO containing cerium under light, Chem. Pap. 76 (2022) 7051–7060, https://doi.org/10.1007/s11696-022-02390-y.

[33] G. Yang, S.J. Park, Conventional and microwave hydrothermal synthesis and application of functional materials: a review, Materials 12 (2019), https://doi.org/10.3390/MA12071177.

[34] S. Baruah, J. Dutta, Hydrothermal growth of ZnO nanostructures, Sci. Technol. Adv. Mater. 10 (2009) 013001, https://doi.org/10.1088/1468-6996/10/1/013001.

[35] B.H. Toby, R.B. Von Dreele, GSAS-II: the genesis of a modern open-source all purpose crystallography software package, Urn:Issn:0021–8898. 46 (2013) 544–549. ⟨https://doi.org/10.1107/S0021889813003531⟩.

[36] S. Mustapha, M.M. Ndamitso, A.S. Abdulkareem, J.O. Tijani, D.T. Shuaib, A. K. Mohammed, A. Sumaila, Comparative study of crystallite size using Williamson-

Hall and Debye-Scherrer plots for ZnO nanoparticles, Adv. Nat. Sci.: Nanosci. Nanotechnol. 10 (2019) 045013, https://doi.org/10.1088/2043-6254/AB52F7.

[37] R. López, R. Gómez, Band-gap energy estimation from diffuse reflectance measurements on sol-gel and commercial TiO 2: a comparative study, J. Sol-Gel Sci. Technol. 61 (2012) 1–7, https://doi.org/10.1007/S10971-011-2582-9/TABLES/2.

[38] WHO global priority pathogens list of antibiotic-resistant bacteria - Combat AMR, (n.d.). ⟨https://www.combatamr.org.au/news-events/who-global-priority-pathogens-list-of-antibiotic-resistant-bacteria⟩ (accessed March 17, 2023).

[39] C.D. Cruz, P. Esteve, P. Tammela, Evaluation and validation of biolog OmniLog® system for antibacterial activity assays, Lett. Appl. Microbiol 72 (2021) 589–595, https://doi.org/10.1111/LAM.13450.

[40] A.J. Moreira, A.C. Borges, B.B. De Sousa, V.R. De Mendonça, C.D. Freschi, G.P. G. Freschi, Photodegradation of fluoxetine applying different photolytic reactors: evaluation of the process efficiency and mechanism, Artic. J. Braz. Chem. Soc. 30 (2019) 1010–1024, https://doi.org/10.21577/0103-5053.20180250.

[41] J.T. Schneider, D.S. Firak, R.R. Ribeiro, P. Peralta-Zamora, Use of scavenger agents in heterogeneous photocatalysis: truths, half-truths, and misinterpretations, Phys. Chem. Chem. Phys. 22 (2020) 15723–15733, https://doi.org/10.1039/D0CP02411B.

[42] A.J. Moreira, J.O.D. Malafatti, T.R. Giraldi, E.C. Paris, E.C. Pereira, V.R. de Mendonça, V.R. Mastelaro, G.P.G. Freschi, Prozac® photodegradation mediated by Mn-doped TiO2 nanoparticles: evaluation of by-products and mechanisms proposal, J. Environ. Chem. Eng. 8 (2020) 104543, https://doi.org/10.1016/j.jece.2020.104543.

[43] X. Wang, C. Sun, S. Gao, L. Wang, H. Shuokui, Validation of germination rate and root elongation as indicator to assess phytotoxicity with cucumis sativus, Chemosphere 44 (2001) 1711–1721, https://doi.org/10.1016/S0045-6535(00)00520-8.

[44] S. Wold, K. Esbensen, P. Geladi, Principal component analysis, Chemom. Intell. Lab. Syst. 2 (1987) 37–52, https://doi.org/10.1016/0169-7439(87)80084-9.

[45] R: A Language and Environment for Statistical Computing, (n.d.). ⟨https://www.gnu.org/copyleft/gpl.html⟩ (accessed August 22, 2023).

[46] K.A. Alim, V.A. Fonoberov, M. Shamsa, Micro-Raman investigation of optical phonons in ZnO nanocrystals, J. Appl. Phys. 97 (2005) 124313, https://doi.org/10.1063/1.1944222.

[47] M.-A. Gatou, N. Lagopati, I.-A. Vagena, M. Gazouli, E.A. Pavlatou, ZnO nanoparticles from different precursors and their photocatalytic potential for biomedical use, Nanomaterials 13 (2022) 122, https://doi.org/10.3390/nano13010122.

[48] M. Gaudon, O. Toulemonde, A. Demourgues, Green coloration of Co-doped ZnO explained from structural refinement and bond considerations, Inorg. Chem. 46 (2007) 10996–11002, https://doi.org/10.1021/ic701157j.

[49] X. Zhang, X. Qian, J. Tang, N. Zhu, Z. Li, J. Fu, L. Li, Y. Wang, Effect of polar/non-polar facets on the transformation of nanoscale ZnO in simulated sweat and potential impacts on the antibacterial activity, Ecotoxicol. Environ. Saf. 246 (2022) 114187, https://doi.org/10.1016/j.ecoenv.2022.114187.

[50] F.H. Abdullah, N.H.H. Abu Bakar, M. Abu Bakar, Current advancements on the fabrication, modification, and industrial application of zinc oxide as photocatalyst in the removal of organic and inorganic contaminants in aquatic systems, (2021). ⟨https://doi.org/10.1016/j.jhazmat.2021.127416⟩.

[51] X. Zhang, J. Qin, Y. Xue, P. Yu, B. Zhang, L. Wang, R. Liu, Effect of aspect ratio and surface defects on the photocatalytic activity of ZnO nanorods, Sci. Rep. 4 (2014) 4596, https://doi.org/10.1038/srep04596.

[52] V. Gerbreders, M. Krasovska, E. Sledevskis, A. Gerbreders, I. Mihailova, E. Tamanis, A. Ogurcovs, Hydrothermal synthesis of ZnO nanostructures with controllable morphology change, CrystEngComm 22 (2020) 1346–1358, https://doi.org/10.1039/C9CE01556F.

[53] G. Murillo, E. Leon-Salguero, P.R. Martínez-Alanis, J. Esteve, J. Alvarado-Rivera, F. Güell, Role of aluminum and HMTA in the hydrothermal synthesis of two-dimensional n-doped ZnO nanosheets, Nano Energy 60 (2019) 817–826, https://doi.org/10.1016/j.nanoen.2019.04.017.

[54] Y. Li, C. Liao, S.C. Tjong, Recent advances in zinc oxide nanostructures with antimicrobial activities, Int. J. Mol. Sci. 21 (2020) 8836, https://doi.org/10.3390/ijms21228836.

[55] V. Gerbreders, M. Krasovska, E. Sledevskis, A. Gerbreders, I. Mihailova, E. Tamanis, A. Ogurcovs, Hydrothermal synthesis of ZnO nanostructures with controllable morphology change, CrystEngComm 22 (2020) 1346–1358, https://doi.org/10.1039/C9CE01556F.

[56] V. Consonni, A.M. Lord, Polarity in ZnO nanowires: a critical issue for piezotronic and piezoelectric devices, Nano Energy 83 (2021), https://doi.org/10.1016/J.NANOEN.2021.105789.

[57] L.A. Gusmão, D.A. Peixoto, J.Z. Marinho, F.C. Romeiro, R.F. Gonçalves, E. Longo, C.A. De Oliveira, R.C. Lima, Alkali influence on ZnO and Ag-doped ZnO nanostructures formation using the microwave-assisted hydrothermal method for fungicidal inhibition, J. Phys. Chem. Solids 158 (2021) 110234, https://doi.org/10.1016/j.jpcs.2021.110234.

[58] R.C. Lima, L.R. Macario, J.W.M. Espinosa, V.M. Longo, R. Erlo, N.L. Marana, J. R. Sambrano, M.L. dos Santos, A.P. Moura, P.S. Pizani, J. Andrés, E. Longo, J. A. Varela, Toward an understanding of intermediate- and short-range defects in ZnO single crystals. A combined experimental and theoretical study, J. Phys. Chem. A 112 (2008) 8970–8978, https://doi.org/10.1021/jp8022474.

[59] D. Mora-Fonz, T. Lazauskas, M.R. Farrow, C.R.A. Catlow, S.M. Woodley, A. A. Sokol, Why are polar surfaces of ZnO stable? Chem. Mater. 29 (2017) 5306–5320, https://doi.org/10.1021/ACS.CHEMMATER.7B01487/ASSET/IMAGES/LARGE/CM-2017-01487P_0010.JPEG.

[60] Synthesis and characterization of copper zinc oxide nanoparticles obtained via metathesis process *, (2017). ⟨https://doi.org/10.1088/2043-6254/aa7223⟩.

[61] S.A. Hassanzadeh-Tabrizi, Precise calculation of crystallite size of nanomaterials: a review, J. Alloy. Compd. 968 (2023) 171914, https://doi.org/10.1016/J.JALLCOM.2023.171914.

[62] L. Qi, K. Wang, Y. Qi, H. Yu, X. Jin, X. Li, Y. Qi, Facile synthesis of ZnO films with anisotropic preferred orientations: An effective strategy for controllable surface and optical property, (2022). ⟨https://doi.org/10.1016/j.jallcom.2022.168125⟩.

[63] M.M. Khan, M.H. Harunsani, A.L. Tan, M. Hojamberdiev, Y.A. Poi, N. Ahmad, Antibacterial studies of ZnO and Cu-doped ZnO nanoparticles synthesized using aqueous leaf extract of stachytarpheta jamaicensis, Bionanoscience 10 (2020) 1037–1048, https://doi.org/10.1007/S12668-020-00775-5/FIGURES/10.

[64] E.S. Asuncion Dimapilis, C.-S. Hsu, R.O. Marie Mendoza, M.-C. Lu, Zinc oxide nanoparticles for water disinfection, (2017). ⟨https://doi.org/10.1016/j.serj.2017.10.001⟩.

[65] P. Pranjali, M.K. Meher, R. Raj, N. Prasad, K.M. Poluri, D. Kumar, A. Guleria, Physicochemical and antibacterial properties of PEGylated zinc oxide nanoparticles dispersed in peritoneal dialysis fluid, ACS Omega 4 (2019) 19255–19264, https://doi.org/10.1021/acsomega.9b02615.

[66] A.E. Nel, L. Mädler, D. Velegol, T. Xia, E.M.V. Hoek, P. Somasundaran, F. Klaessig, V. Castranova, M. Thompson, Understanding biophysicochemical interactions at the nano–bio interface, Nat. Mater. 8 (7) (2009) 543–557, https://doi.org/10.1038/nmat2442.

[67] M. Rajagopal, S. Walker, Envelope structures of gram-positive bacteria, Curr. Top. Microbiol Immunol. 404 (2017) 1, https://doi.org/10.1007/82_2015_5021.

[68] C. Hutchings, Z.P. Yair, R. Reifen, M. Shemesh, Antimicrobial effect of zn2+ ions governs the microbial quality of donor human milk, Foods 10 (2021), https://doi.org/10.3390/foods10030637.

[69] K.R. Raghupathi, R.T. Koodali, A.C. Manna, Size-dependent bacterial growth inhibition and mechanism of antibacterial activity of zinc oxide nanoparticles, Langmuir 27 (2011) 4020–4028, https://doi.org/10.1021/LA104825U/ASSET/IMAGES/LARGE/LA-2010-04825U_0004.JPEG.

[70] C.R. Mendes, G. Dilarri, C.F. Forsan, V. de R. Sapata, P.R.M. Lopes, P.B. de Moraes, R.N. Montagnolli, H. Ferreira, E.D. Bidoia, Antibacterial action and target mechanisms of zinc oxide nanoparticles against bacterial pathogens, Sci. Rep. 12 (1) (2022) 1–10, https://doi.org/10.1038/s41598-022-06657-y.

[71] S. Halder, K.K. Yadav, R. Sarkar, S. Mukherjee, P. Saha, S. Haldar, S. Karmakar, T. Sen, Alteration of Zeta potential and membrane permeability in bacteria: a study with cationic agents, Springerplus 4 (2015) 1–14, https://doi.org/10.1186/S40064-015-1476-7/FIGURES/4.

[72] A. Singh, N.B. Singh, S. Afzal, T. Singh, I. Hussain, Zinc oxide nanoparticles: a review of their biological synthesis, antimicrobial activity, uptake, translocation and biotransformation in plants, J. Mater. Sci. 53 (2018) 185–201, https://doi.org/10.1007/s10853-017-1544-1.

[73] S. Brown, J.P. Santa Maria, S. Walker, Wall teichoic acids of gram-positive bacteria, Annu. Rev. Microbiol. 67 (2013) 313–336, https://doi.org/10.1146/ANNUREV-MICRO-092412-155620.

[74] N. Babayevska, Ł. Przysiecka, I. Iatsunskyi, G. Nowaczyk, M. Jarek, E. Janiszewska, S. Jurga, ZnO size and shape effect on antibacterial activity and cytotoxicity profile, Sci. Rep. 12 (2022) 1–13, https://doi.org/10.1038/s41598-022-12134-3.

[75] S. Nagarajan, K. Arumugam Kuppusamy, Extracellular synthesis of zinc oxide nanoparticle using seaweeds of gulf of Mannar, India, J. Nanobiotechnol. 11 (2013) 39, https://doi.org/10.1186/1477-3155-11-39.

[76] S. Ashikuzzaman Ayon, M. Jamal, M. Muktadir Billah, S. Neaz, Augmentation of magnetic properties and antimicrobial activities of band gap modified Ho 3+ and Sm 3+ doped ZnO nanoparticles: A comparative experimental study, (2021). ⟨https://doi.org/10.1016/j.jallcom.2021.163179⟩.

[77] Y. Li, W. Zhang, J. Niu, Y. Chen, Mechanism of Photogenerated Reactive Oxygen Species and Correlation with the Antibacterial Properties of Engineered Metal-Oxide Nanoparticles, (2012). ⟨https://doi.org/10.1021/nn300894k⟩.

[78] J. Du, J.M. Gebicki, Proteins are major initial cell targets of hydroxyl free radicals, Int J. Biochem Cell Biol. 36 (2004) 2334–2343, https://doi.org/10.1016/j.biocel.2004.05.012.

[79] P. Makuła, M. Pacia, W. Macyk, How to correctly determine the band gap energy of modified semiconductor photocatalysts based on UV-vis spectra, J. Phys. Chem. Lett. 9 (2018) 6814–6817, https://doi.org/10.1021/ACS.JPCLETT.8B02892/SUPPL_FILE/JZ8B02892_LIVESLIDES.MP4.

[80] J.Sen Chang, J. Strunk, M.N. Chong, P.E. Poh, J.D. Ocon, Multi-dimensional zinc oxide (ZnO) nanoarchitectures as efficient photocatalysts: what is the fundamental factor that determines photoactivity in ZnO? J. Hazard Mater. 381 (2020) 120958 https://doi.org/10.1016/j.jhazmat.2019.120958.

[81] A.J. Moreira, J.O.D. Malafatti, T.R. Giraldi, E.C. Paris, E.C. Pereira, V.Romito De Mendonça, R. Mastelaro, G.P.G. Freschi, Prozac® photodegradation mediated by Mn-doped TiO 2 nanoparticles: evaluation of by-products and mechanisms proposal, J. Environ. Chem. Eng. 8 (2020) 2213–3437, https://doi.org/10.1016/j.jece.2020.104543.

[82] F.M. Albarakaty, M.I. Alzaban, N.K. Alharbi, F.S. Bagrwan, A.R.M. Abd El-Aziz, M. A. Mahmoud, Zinc oxide nanoparticles, biosynthesis, characterization and their potent photocatalytic degradation, and antioxidant activities, J. King Saud. Univ. Sci. 35 (2023) 102434, https://doi.org/10.1016/J.JKSUS.2022.102434.

[83] O.J. Nava, P.A. Luque, C.M. Gómez-Gutiérrez, A.R. Vilchis-Nestor, A. Castro-Beltrán, M.L. Mota-González, A. Olivas, Influence of camellia sinensis extract on zinc oxide nanoparticle green synthesis, J. Mol. Struct. 1134 (2017) 121–125, https://doi.org/10.1016/j.molstruc.2016.12.069.

[84] A. Balcha, O.P. Yadav, T. Dey, Photocatalytic degradation of methylene blue dye by zinc oxide nanoparticles obtained from precipitation and sol-gel methods,

Environ. Sci. Pollut. Res. 23 (2016) 25485–25493, https://doi.org/10.1007/S11356-016-7750-6/FIGURES/11.

[85] R. Perez-Cuapio, J. Alberto Alvarado, H. Juarez, H.-J. Sue, Sun irradiated high efficient photocatalyst ZnO nanoparticles obtained by assisted microwave irradiation, Mater. Sci. Eng.: B 289 (2023) 116263, https://doi.org/10.1016/j.mseb.2023.116263.

[86] A. Raja, S. Ashokkumar, R. Pavithra Marthandam, J. Jayachandiran, C. P. Khatiwada, K. Kaviyarasu, R. Ganapathi Raman, M. Swaminathan, Eco-friendly preparation of zinc oxide nanoparticles using Tabernaemontana divaricata and its photocatalytic and antimicrobial activity, J. Photochem. Photobio. B 181 (2018) 53–58, https://doi.org/10.1016/j.jphotobiol.2018.02.011.

[87] R. Zhang, H. Zhang, C. Tu, X. Hu, L. Li, Y. Luo, P. Christie, Phytotoxicity of ZnO nanoparticles and the released Zn(II) ion to corn (Zea mays L.) and cucumber (Cucumis sativus L.) during germination, Environ. Sci. Pollut. Res. 22 (2015) 11109–11117, https://doi.org/10.1007/S11356-015-4325-X/FIGURES/5.

[88] C. García-Gómez, M. Babin, A. Obrador, J.M. Álvarez, M.D. Fernández, Integrating ecotoxicity and chemical approaches to compare the effects of ZnO nanoparticles, ZnO bulk, and ZnCl2 on plants and microorganisms in a natural soil, Environ. Sci. Pollut. Res. 22 (2015) 16803–16813, https://doi.org/10.1007/S11356-015-4867-Y/FIGURES/5.

[89] C. García-Gómez, A. Obrador, D. González, M. Babín, M.D. Fernández, Comparative study of the phytotoxicity of ZnO nanoparticles and Zn accumulation in nine crops grown in a calcareous soil and an acidic soil, Sci. Total Environ. 644 (2018) 770–780, https://doi.org/10.1016/J.SCITOTENV.2018.06.356.

[90] I. Bragança, P.C. Lemos, P. Barros, C. Delerue-Matos, V.F. Domingues, Phytotoxicity of pyrethroid pesticides and its metabolite towards Cucumis sativus, (2017). ⟨https://doi.org/10.1016/j.scitotenv.2017.11.164⟩.

[91] C.A. Demarchi, L.Mota Da Silva, A. Ślawska-Waniewska, N. Nedelko, J. Dal Magro, J. Scapinello, C.A. Rodrigues, Phytotoxicity study of Ag@Fe 2 O 3 nanocomposites based on O-carboxymethylchitosan on Cucumis sativus, (2019). ⟨https://doi.org/10.1016/j.jece.2019.102890⟩.